bioRxiv preprint doi: https://doi.org/10.1101/2022.04.30.490180; this version posted May 1, 2022. The copyright holder for this preprint (which was not certified by peer review) is the author/funder, who has granted bioRxiv a license to display the preprint in perpetuity. It is made available under aCC-BY-NC-ND 4.0 International license.

# Transcription-induced active forces suppress chromatin motion by inducing a transient disorder-to-order transition

Sucheol Shin,[1] Hyun Woo Cho,[2] Guang Shi,[1,3] and D. Thirumalai[1,*]

[1] *Department of Chemistry, The University of Texas at Austin, Texas 78712, USA*
[2] *Department of Fine Chemistry and Center for Functional Biomaterials, Seoul National University of Science and Technology, Seoul 01811, Republic of Korea*
[3] *Department of Materials Science, University of Illinois, Urbana, Illinois 61801, USA*

(Dated: April 30, 2022)

Recent experiments have shown that the mobility of human interphase chromosome decreases during transcription, and increases upon inhibiting transcription, a finding that is counter-intuitive because it is thought that the active mechanical force ($F$) generated by RNA polymerase II (RNAPII) on chromatin would render it more open and mobile. We use a polymer model to investigate how $F$, derived from transcriptional activity, affects the dynamical properties of chromatin. The movements of the loci in the gene-rich region are suppressed in an intermediate range of $F$, and are enhanced at small and large $F$ values. In the intermediate $F$, the bond length between consecutive loci increases, becoming commensurate with the location of the minimum in the attractive interaction between the active loci in the chromatin. This results in a disorder-to-order transition, leading to the decreased mobility during transcription. Our results suggest that transient ordering of the loci in the gene-rich region might be a mechanism for nucleating a dynamic network involving transcription factors, RNAPII, and chromatin.

Advances in experimental techniques [1, 2] have elucidated the organizational details of chromosomes, thus deepening our understandings of how gene regulation is connected to chromatin structure [3]. In contrast, much less is known about the dynamics of the densely packed interphase chromosomes in the cell nucleus. Experimental and theoretical studies have shown that the locus dynamics is massively heterogeneous, exhibiting subdiffusive behavior [4–7]. In addition, physical models of chromosomes [8–10] predict glass-like dynamics at the level of the individual locus in interphase chromosomes. However, it is challenging to understand the dynamic nature of chromosomes that govern the complex subnuclear processes, such as gene transcription.

The link between transcription activity and changes in chromosomal dynamics is important in understanding the dynamics of chromosomes in distinct cell types and states [11, 12]. It is reasonable to expect that transcription of the active gene-rich region could make it more expanded and dynamic [13, 14]. It, therefore, is surprising that active RNA polymerase (RNAP) II suppressed the movement of the gene-rich euchromatin nucleosomes [12]. Let us first summarize the key experimental results, which we used as a springboard to launch our study: (1) By imaging the motion of individual nucleosomes in live human cells, it was shown that the mean square displacements (MSDs) of the nucleosomes during active transcription are constrained (Fig. S1 [15]). (2) When the cells were treated with $\alpha$-amanitin ($\alpha$-AM) or 5,6-dichloro-1-$\beta$-D-ribofuranosylbenzimidazole (DRB), both of which selectively block the translocation of RNAPII [16, 17], the mobility of the nucleosomes was enhanced. This finding is counter-intuitive because one expects that the elongation process of RNAP generates mechanical forces [18, 19], that could render the chromatin region to be open and dynamic. (3) The enhanced motion was restricted only to euchromatin loci that are predominantly localized in the cell interior whereas the dynamics of heterochromatin, found mostly in the periphery, is unaffected by transcription. Based on these observations, it was hypothesized that RNAPs and other protein complexes, facilitating transcription, transiently stabilize chromatin by forming dynamic clusters, referred to as transcription factories [20–23]. This hypothesis is, however, challenged by the observation that inhibition by DRB mainly leads to stalling of RNAPs while they are still bound on chromatin [17]. Moreover, it turns out that transcriptional inhibition does not significantly alter the higher-order structures of the chromosomes [23, 24]. These observations raise the question: Is there a physical explanation for the increased chromatin dynamics upon inhibition of transcription and a decrease during transcription? We provide a plausible answer to this question using a minimal model.

Using the experimental results as a backdrop, we theorize that RNAPII exerts active force in a vectorial manner on the active loci. We then examine the effects of active force using the Chromosome Copolymer Model (CCM) [9]. The CCM, with only one energy scale, faithfully captures the Hi-C experimental results, showing microphase separation between euchromatin (A-type loci) and heterochromatin (B-type loci) on large length scale and formation of topologically associating domains on a smaller length scale in interphase chromosomes. Here, we perform Brownian dynamics simulations of the CCM with active force in order to model the mechanical effects due to transcriptional elongation. Our major results are: (i) The dynamics of the active loci, measured using

bioRxiv preprint doi: https://doi.org/10.1101/2022.04.30.490180; this version posted May 1, 2022. The copyright holder for this preprint (which was not certified by peer review) is the author/funder, who has granted bioRxiv a license to display the preprint in perpetuity. It is made available under aCC-BY-NC-ND 4.0 International license.



the MSD, is suppressed upon application of the active force, which is in accord with experiments [12]. Interestingly, the relative increase in the MSD with respect to the transcriptionally inactive case, is in near quantitative agreement with experiments. (ii) The changes in the MSD only affect the A-type loci but not the B-type loci, even though the chromosome is a copolymer linking A and B loci. (iii) The decrease in the A-type loci mobility occurs only over a range of activity level. Surprisingly, in this range the segregated A-loci undergo a transient disorder-to-order transition, resembling a face-centered cubic (FCC) lattice, whereas the B-type loci are fluid-like.

We model an interphase chromosome as a flexible self-avoiding copolymer (Fig. 1) [15]. Non-adjacent pairs of loci are subject to favorable interactions, modeled by the Lennard-Jones (LJ) potential, depending on the locus type. The interactions between the loci, whose relative strength is constrained by the Flory-Huggins theory [25, 26], ensure microphase separation between the A and B loci. Additionally, specific locus pairs are anchored to each other, thus representing the chromatin loops mediated by CTCFs [27]. In this study, a 4.8-Mbp segment of human chromosome 5 is coarse-grained using $N = 4{,}000$ loci (1.2 kbp per locus). The A- to B-type ratio is $N_{\rm A}/N_{\rm B} = 982/3018 \approx 1/3$ [15].

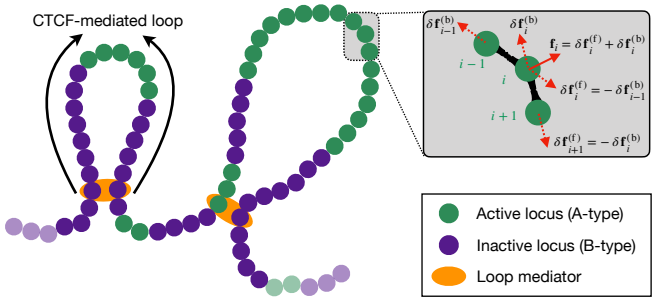


FIG. 1. Schematic depiction of the CCM. Chromosome is modeled as a copolymer chain consisting of active/inactive (green/purple-colored) loci. Specific locus pairs are connected to each other by loop mediators (orange color). The gray box on the right illustrates how active forces are imposed on $i^{\rm th}$ locus and its bonded loci (see the main text for details). We apply active forces only on the gene-rich A-type loci.

We applied active forces on the chain to model force generation during transcription. Previous theoretical studies [28–30], with the possible exception [31], have considered different forms of active forces on homopolymers, without making connections to experiments. Because the translocation of RNAP and the nucleosome sliding gives rise to tensional force [18, 19], we model the active force in an extensile manner along each bond vector of the A-type loci, ensuring momentum conservation (dotted arrows in the gray box of Fig. 1). For the bond vector, $\mathbf{b}_i = \mathbf{r}_{i+1} - \mathbf{r}_i$, force, $\delta\mathbf{f}^{(\rm f)}_{i+1} = f_0\hat{\mathbf{b}}_i$, is exerted on $(i+1)^{\rm th}$ locus in the forward direction, where $f_0$ is the force magnitude and $\hat{\mathbf{b}}_i = \mathbf{b}_i/|\mathbf{b}_i|$, and $\delta\mathbf{f}^{(\rm b)}_i = -\delta\mathbf{f}^{(\rm f)}_{i+1}$ is exerted on the $i^{\rm th}$ locus in the backward direction.We use the dimensionless parameter, $F \equiv f_0\sigma/k_BT$, as a measure of the force magnitude, where $\sigma$ is the diameter of a single locus, $k_B$ is the Boltzmann constant, and $T$ is the temperature.

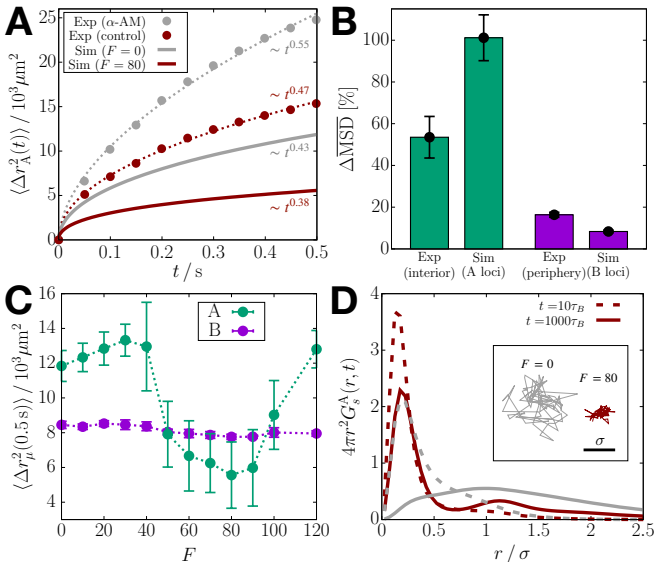


FIG. 2. Transcription-induced active forces reduce the euchromatin mobility. (A) $\langle\Delta r^2_{\rm A}(t)\rangle$ [Eq. (1)] from simulations with $F = 0$ and $F = 80$ (solid lines), compared with the euchromatin MSD from the experiment that inhibits transcription using $\alpha$-AM [12] (circles). The dotted lines are the fits to the experimental data. (B) Bar graphs comparing the increase in $\langle\Delta r^2_{\rm A}(t)\rangle$ ($\langle\Delta r^2_{\rm B}(t)\rangle$) shown in panel A (Fig. S2A) between experiment and simulation results. (C) MSDs for the A and B loci at $t = 0.5$ s as a function of $F$. The dotted lines are a guide to the eye. (D) Radial distributions of the A-locus displacement at different lag times, $t = 10\tau_B$ (dashed) and $t = 1{,}000\tau_B$ (solid), compared between $F = 0$ (gray) and $F = 80$ (dark-red). The inset shows the 2-D projection of the trajectory of an active locus for $10^4\tau_B$ at $F = 0$ and $F = 80$.

We performed Brownian dynamics simulations, as described in detail elsewhere [15]. We calculated the MSDs separately for euchromatin and heterochromatin loci,

$$\langle\Delta r^2_\mu(t)\rangle = \frac{1}{N_\mu}\left\langle\sum_{i=1}^{N}\delta_{\nu(i)\mu}|\mathbf{r}_i(t)-\mathbf{r}_i(0)|^2\right\rangle , \quad (1)$$

where $\delta_{\nu(i)\mu}$ is the Kronecker delta ($\mu$ =A or B), and $\langle\cdots\rangle$ is the ensemble average. Data analysis and other details are in the Supplemental Material [15]. Fig. 2A shows that, $\langle\Delta r^2_{\rm A}(t)\rangle$ is smaller with $F = 80$ compared to $F = 0$. This result is comparable to the nucleosome MSDs measured from the interior section of the cell nucleus treated with the transcription inhibitor $\alpha$-AM [12]. Our simulations capture the change in the scaling exponent, $\alpha$, extracted from $\langle\Delta r^2_\mu(t)\rangle \sim t^\alpha$ [$\Delta\alpha$(active $\rightarrow$

bioRxiv preprint doi: https://doi.org/10.1101/2022.04.30.490180; this version posted May 1, 2022. The copyright holder for this preprint (which was not certified by peer review) is the author/funder, who has granted bioRxiv a license to display the preprint in perpetuity. It is made available under aCC-BY-NC-ND 4.0 International license.



passive) = 0.05 versus 0.08]. However, the magnitude of $\langle \Delta r_{\rm A}^2(t)\rangle$ is smaller in simulations than in experiment. $\langle \Delta r_{\rm B}^2(t)\rangle$ at $F = 80$ is also smaller than at $F = 0$, but the difference is marginal compared to $\langle \Delta r_{\rm A}^2(t)\rangle$, which is consistent with the experimental results for the nuclear periphery (Fig. S2A). We could have obtained better agreement with experiments by tweaking the parameters in the model. We did not do so because our goal is to uncover the mechanism underlying the enhancement in the MSD upon inhibiting transcription.

In Fig. 2B, we compare the transcription inhibited increase ($\Delta\overline{\rm MSD}$) in the MSD, between experiment and simulations (see Eqs. (S7)-(S8) [15]). We use $F = 80$, which has the smallest MSD (see Fig. 2C), as the control. The value of $f_0$ for $F = 80$ is in the range, $f_0 \approx$ 3-16 pN [15], which accords well with forces exerted by RNAP [18]. Comparison between $\Delta\overline{\rm MSD}$ for the A loci (simulation) and the interior measurements (experiment) is less quantitative than between the B loci and the periphery. This difference may arise because the interior measurements could include the heterochromatin contribution to some extent, whereas the periphery measurements exclude the euchromatin. Nevertheless, we observe that $\Delta\overline{\rm MSD}$ for all the loci are in near quantitative agreement with experiment, especially for $\Delta\overline{\rm MSD}$ for DRB (Fig. S2C). The good agreement between simulations and experiment is surprising because it is obtained *without adjusting any parameter to fit the data*. Although comparison between simulations and experiments in Fig. 2B is made with $F = 80$, we obtain qualitatively similar results for $F$ in the range, $60 \le F \le 90$ (Fig. S3).

The simulated MSD, at a given time, changes non-monotonically with respect to $F$. Remarkably, the change is confined to the A loci (Figs. 2C and S2D-S2E); $\langle \Delta r_{\rm A}^2(0.5\,{\rm s})\rangle$ increases modestly as $F$ increases from zero to $F \lesssim 30$, and decreases when $F$ exceeds thirty. There is an abrupt reduction at $F \approx 50$. In the range, $50 \lesssim F \lesssim 80$, $\langle \Delta r_{\rm A}^2(0.5\,{\rm s})\rangle$ continues to decrease before an increase at higher $F$ values. We also calculated the van Hove function, $G_s^{\mu}(\mathbf{r},t) = \left\langle \sum_{i=1}^{N} \delta_{\nu(i)\mu}\delta(\mathbf{r}+\mathbf{r}_i(0)-\mathbf{r}_i(t))\right\rangle / N_\mu$, at $t = 10\tau_B \approx 0.007\,$s and $1000\tau_B \approx 0.7\,$s [32]. The A-type loci at $F = 80$ do not diffuse as much at $F = 0$ (Fig. 2D), and their displacements are largely within the length scale of $\sigma$. In contrast, there is no significant difference in $G_s^{\rm B}(r,t)$ between $F = 0$ and $F = 80$ (Fig. S2F). Notably, the second peak of $G_s^{\rm A}(r,t)$ at $F = 80$ hints at the solid-like lattice [33], which is revealed below.

To probe the extent to which glass-like behavior [5, 8, 9] is preserved in the presence of RNAPII-induced active forces, we calculated the self-intermediate scattering function,

$$F_s(|\mathbf{k}|,t) = \frac{1}{N}\sum_{j=1}^{N} e^{i\mathbf{k}\cdot[\mathbf{r}_j(t)-\mathbf{r}_j(0)]}\ , \qquad (2)$$

where $\mathbf{k}$ is the wave vector. We computed, $\langle F_s(k_{\rm max},t)\rangle$

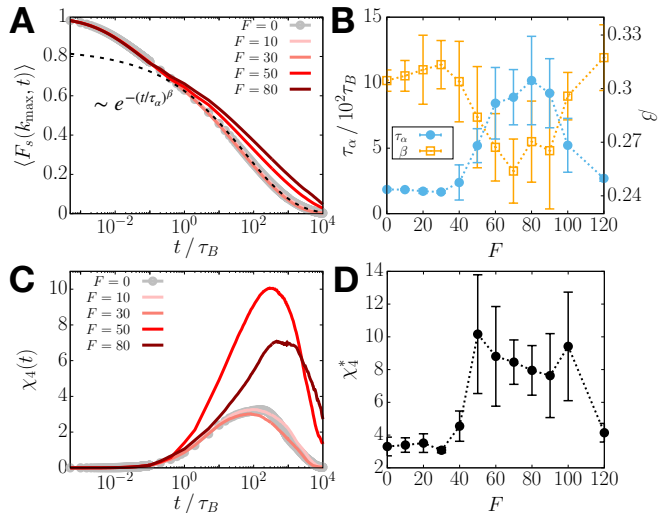


FIG. 3. Active force increases the relaxation time and dynamic heterogeneity. (A) Plot of $\langle F_s(k_{\rm max},t)\rangle$ [Eq. (2)] for different $F$. The dashed line is a stretched exponential fit for $F = 0$. (B) $\tau_\alpha$ (blue) and $\beta$ (orange) of $\langle F_s(k_{\rm max},t)\rangle$ as a function of $F$. The dotted lines are a guide to the eye. (C) Plot of $\chi_4(t)$ [Eq. (3)] for different $F$. (D) The maximum value of $\chi_4(t)$ as a function of $F$.

($k_{\rm max} = 2\pi/\sigma$), whose decay indicates the structural relaxation. Time-dependent variations in $\langle F_s(k_{\rm max},t)\rangle$ (Fig. 3A) show stretched exponential behavior ($e^{-(t/\tau_a)^\beta}$; $\beta < 1/3$ at all $F$ values), which is one signature of glass-like dynamics. The decay is even slower if $F$ is increased. The relaxation time, $\tau_\alpha$, calculated using $\langle F_s(k_{\rm max},\tau_\alpha)\rangle = 0.2$, shows that the relaxation is slowest at $F \approx 80$ (Fig. 3B), which occurs after the dynamical transition in $\langle \Delta r_{\rm A}^2(0.5\,{\rm s})\rangle$ at $F \approx 50$ and before $\langle \Delta r_{\rm A}^2(0.5\,{\rm s})\rangle$ increases beyond $F = 100$ (Fig. 2C). Similarly, when the tails of $\langle F_s(k_{\rm max},t)\rangle$ were fit with $e^{-(t/\tau_a)^\beta}$, the exponent $\beta$ also exhibits the analogous trend (Fig. 3B). As $\tau_\alpha$ increases, $\beta$ decreases.

Dynamic heterogeneity, another hallmark of glass-like dynamics [34, 35], was calculated using the fourth-order susceptibility [36],

$$\chi_4(t) = N\left[\left\langle F_s(k_{\rm max},t)^2\right\rangle - \left\langle F_s(k_{\rm max},t)\right\rangle^2\right]\ . \qquad (3)$$

$\chi_4(t)$ has a broad peak spanning a wide range of times, reflecting the heterogeneous motion of the loci (Fig. 3C). The peak height, $\chi_4^*$, increases till $F \approx 50$ and subsequently decreases (Fig. 3D). When $F$ exceeds 100, $\chi_4^*$ decreases precipitously. Our results suggest that there are two transitions: one at $F \approx 50$ where the dynamics slows down and the other, which is a reentrant transition beyond $F = 100$, signaled by an enhancement in the loci mobility. Although the system is finite, these transitions are discernible.

Like the MSD, when $\langle F_s(k_{\rm max},t)\rangle$ and $\chi_4(t)$ was decomposed into the contributions from A and B loci, we

bioRxiv preprint doi: https://doi.org/10.1101/2022.04.30.490180; this version posted May 1, 2022. The copyright holder for this preprint (which was not certified by peer review) is the author/funder, who has granted bioRxiv a license to display the preprint in perpetuity. It is made available under aCC-BY-NC-ND 4.0 International license.



find that the decrease in the dynamics and the enhanced heterogeneity are driven by the active loci (Fig. S4). These observations, including the non-monotonicity in $\tau_\alpha$ and $\beta$ that exhibit a dynamic reentrant behavior, prompted us to examine if the dynamical changes in the A-type loci are accompanied by any structural alterations.

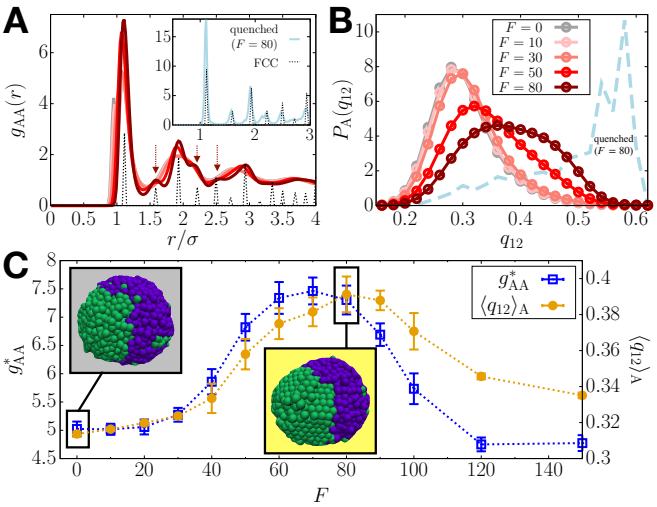


FIG. 4. Crystallization due to active force, $F$. (A) RDF for A-A locus pairs at different $F$ (solid lines; see the legend in panel B), where $g(r)$ for a FCC crystal is shown with the dotted line (scaled arbitrarily). The inset shows inherent structure $g_{AA}(r)$ for the quenched polymer with $F = 80$. (B) Distributions of the BOO parameter, $q_{12}$, for A loci as a function of $F$. The dashed line is for the quenched A loci at $F = 80$. (C) Height of the dominant peak in $g_{AA}(r)$ (blue) and $\langle q_{12}\rangle_A$ (orange) as a function of $F$. Simulation snapshots for $F = 0$ and $F = 80$ are displayed in the gray- and yellow-background boxes, respectively. The A and B loci are shown in green and purple spheres, respectively.

The radial distribution function (RDF) for A-A locus pairs, $g_{AA}(r)$, with signature of a dense fluid, shows no visible change for $F \lesssim 30$ (Fig. 4A). In sharp contrast, the height of the primary peak, $g^*_{AA}$, increases sharply beyond $F = 30$ (Fig. 4C). Remarkably, $g_{AA}(r)$ for $F = 80$ exhibits secondary peaks that are characteristics of a FCC-like solid (arrows, Fig. 4A). Upon further increase in $F$, these peaks disappear (Fig. S5A) and $g^*_{AA}$ reverts to the level of the passive case (Fig. 4C). In other words, the active forces, which preserve fluid-like disorder in the A-type loci at low $F$ values, induce a structural transition to FCC-like order in the intermediate range of $F$ values, which is followed by reentrance to a fluid-like behavior at higher $F$ values. In contrast, $g_{BB}(r)$ exhibits dense fluid-like behavior at all $F$ values (Fig. S5B). We confirm that the FCC lattice is the minimum energy configuration by determining the *inherent structure* for the A loci at $F = 80$ by quenching the active polymer to a low temperature [15, 37, 38] (Fig. 4A, inset). Quenching does not alter the structure of the B loci at $F = 80$ or $g_{AA}(r)$ at $F = 0$ (Figs. S5C-S5D).

To assess the local order in the A-type loci, we calculated the bond-orientational order (BOO) parameter for 12-fold rotational symmetry, $q_{12}$ [15, 39, 40]. For a perfect FCC crystal, $q_{12} \approx 0.6$ [41]. The distribution for A loci, $P_A(q_{12})$, is centered around $q_{12} = 0.3$ at $F = 0$ (Fig. 4B), representing a disordered liquid state (gray box, Fig. 4C). As $F$ is increased, the distribution shifts towards the right especially in the $50 \leq F \leq 80$ range. The increase of $\langle q_{12}\rangle_A$ indicates a transition to a FCC-like ordered state that is visible in the simulations (yellow box, Fig. 4C). Although $P_A(q_{12})$ at $F = 80$ is broad due to thermal fluctuations, the inherent structure gives a narrower distribution, peaked near $q_{12} = 0.6$ (dashed line, Fig. 4B). The maximum in $P_A(q_{12})$ shifts to the left for $F > 80$ (Fig. S5E) and $\langle q_{12}\rangle_A$ decreases, suggestive of $F$-induced reentrant transition. The distribution $P_B(q_{12})$ for the B-type loci is independent of $F$ (Fig. S5F). These results show that FCC-like ordering emerges in $50 \lesssim F \lesssim 100$ range. Outside this range, the RDFs display the characteristics of a dense fluid for the condensed chromosome. The transitions in the A-type loci may be summarized as fluid $\rightarrow$ FCC $\rightarrow$ fluid, as $F$ changes from 0 to 120.

The emergence of FCC-like order in the A-type loci can be understood using the effective A-A interaction generated by $F$. Since $F$ is exerted on each A-A bond (Fig. 1), the force increases the distances between the bonded A-A pairs. We calculated the *effective* pair potential for an A-A bond, $u_b^{\rm eff}(r) = u_b^0(r) - f_0(r - b_0)$, where $u_b^0(r)$ and $b_0$ are the $F$-independent bonding potential, and the corresponding equilibrium bond length, respectively. The $f_0(r - b_0)$ term represents the work done by the active force to stretch the bond from $b_0$. The equation of motion for $F \neq 0$ involves the effective potential, $u_b^{\rm eff}(r)$ [15]. Plots of $u_b^{\rm eff}(r)$ in Fig. 5A show that the effective equilibrium bond length, $r_{\rm min}$, increases as $F$ increases. This prediction is confirmed by the direct measurement of A-A bond distance from the simulations (Figs. S6A-S6B). Note that $r_{\rm min}(F = 80) \approx r^*_{\rm LJ} \approx 1.12\sigma$, where $r^*_{\rm LJ}$ is the distance at the minimum of the LJ potential (Fig. 5B). The $F$-induced extension of A-A bonds makes the A-A bond distances commensurate with $r^*_{\rm LJ}$, which is conducive to FCC ordering [42] in the active loci.

We can also describe the ordering behavior using thermodynamic properties based on $u_b^{\rm eff}(r)$. We calculated the mean and variance of $E_{\rm eff,A}$ [15]. Fig. 5C shows that $\langle E_{\rm eff,A}\rangle$ decreases smoothly as $F$ changes, without pronounced change in the slope, as might be expected for a structural transition [43]. Nevertheless, $\langle(\delta E_{\rm eff,A})^2\rangle$ indicates signatures of a transition more dramatically, with peaks at $F = 50$ and $F = 100$ (arrows I and II, Fig. 5C). Thus, both ordering and reentrant fluid behavior coincide with the boundaries of the dynamic transitions noted in Figs. 2B, 3B, and 3D.

To ascertain the robustness of our results, we per-

bioRxiv preprint doi: https://doi.org/10.1101/2022.04.30.490180; this version posted May 1, 2022. The copyright holder for this preprint (which was not certified by peer review) is the author/funder, who has granted bioRxiv a license to display the preprint in perpetuity. It is made available under aCC-BY-NC-ND 4.0 International license.



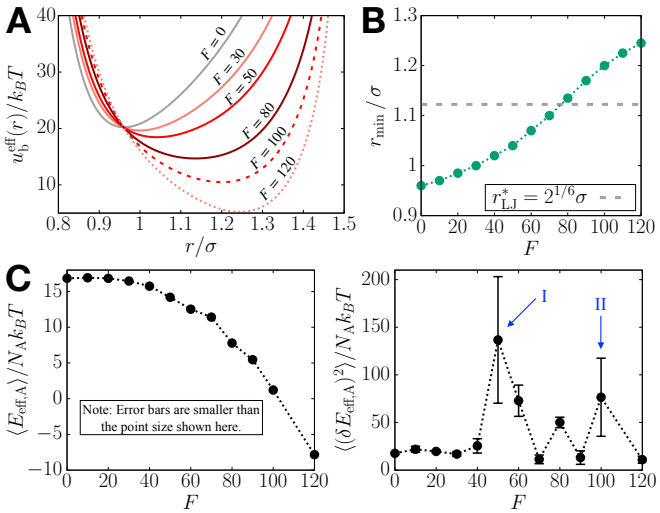


FIG. 5. Effective potential energy accounts for the crystallization of the A-type loci. (A) Effective pair potential of a single A-A bond, $u_b^{eff}(r)$, as a function of $F$. (B) Distance at the minimum of $u_b^{eff}(r)$ as a function of $F$, where the minimum distance for the non-bonding pair potential is shown by the dashed line. (C) Mean of the effective potential energy of A loci (left) and mean fluctuations (right) with respect to $F$. The arrows indicate the two structural transitions.

formed simulations for a segment of chromosome 10 with the same length but with a larger fraction of active loci. The behavior is qualitatively similar, except for greater extent of retardation in the dynamics at $F \neq 0$ (Fig. S7). In contrast, for a copolymer chain whose A/B sequence is random, $F$ does not result in ordering transition (Fig. S8). Thus, $F$-induced decrease in the motion of the A-type loci, accompanied by transient ordering, occurs only in copolymer chains with the microphase separation between A and B loci—intrinsic property of interphase chromosomes [44].

We have discovered a novel mechanism for the dynamical changes upon transcriptional inhibition in mammalian interphase chromosomes, which tidily explains the experimental results. Since the transcription is a stochastic process with intermittent pauses [45, 46], the life time of the ordered phase is short, and glass-like phase emerges upon transcription inhibition (Figs. S10-S11).

We thank Xin Li, Davin Jeong, Kiran Kumari, and Bin Zhang for useful discussions. This work was supported by a grant from the National Science Foundation (CHE19-000033) and the Welch Foundation through the Collie-Welch Chair (F-0019).

* Corresponding author: dave.thirumalai@gmail.com

[1] E. Lieberman-Aiden, N. L. van Berkum, L. Williams, M. Imakaev, T. Ragoczy, A. Telling, I. Amit, B. R. Lajoie, P. J. Sabo, M. O. Dorschner, R. Sandstrom, B. Bernstein, M. A. Bender, M. Groudine, A. Gnirke, J. Stamatoyannopoulos, L. A. Mirny, E. S. Lander, and J. Dekker, Science **326**, 289 (2009).
[2] B. Bintu, L. J. Mateo, J.-H. Su, N. A. Sinnott-Armstrong, M. Parker, S. Kinrot, K. Yamaya, A. N. Boettiger, and X. Zhuang, Science **362**, eaau1783 (2018).
[3] E. H. Finn and T. Misteli, Science **365**, eaaw9498 (2019).
[4] I. Bronshtein, E. Kepten, I. Kanter, S. Berezin, M. Lindner, A. B. Redwood, S. Mai, S. Gonzalo, R. Foisner, Y. Shav-Tal, and Y. Garini, Nat. Commun. **6**, 8044 (2015).
[5] L. Liu, G. Shi, D. Thirumalai, and C. Hyeon, PLOS Comput. Biol. **14**, e1006617 (2018).
[6] S. S. Ashwin, T. Nozaki, K. Maeshima, and M. Sasai, Proc. Natl. Acad. Sci. U.S.A. **116**, 19939 (2019).
[7] H. A. Shaban, R. Barth, L. Recoules, and K. Bystricky, Genome Biol **21**, 95 (2020).
[8] H. Kang, Y.-G. Yoon, D. Thirumalai, and C. Hyeon, Phys. Rev. Lett. **115**, 198102 (2015).
[9] G. Shi, L. Liu, C. Hyeon, and D. Thirumalai, Nat. Commun. **9**, 3161 (2018).
[10] M. Di Pierro, D. A. Potoyan, P. G. Wolynes, and J. N. Onuchic, Proc. Natl. Acad. Sci. U.S.A. **115**, 7753 (2018).
[11] T. Nozaki, R. Imai, M. Tanbo, R. Nagashima, S. Tamura, and T. Tani, Mol. Cell **67**, 282 (2017).
[12] R. Nagashima, K. Hibino, S. S. Ashwin, M. Babokhov, S. Fujishiro, R. Imai, T. Nozaki, S. Tamura, T. Tani, H. Kimura, M. Shribak, M. T. Kanemaki, M. Sasai, and K. Maeshima, J. Cell Biol. **218**, 1511 (2019).
[13] B. Gu, T. Swigut, A. Spencley, M. R. Bauer, M. Chung, T. Meyer, and J. Wysocka, Science **359**, 1050 (2018).
[14] M. M. Tortora, H. Salari, and D. Jost, Curr. Opin. Genet. Dev. **61**, 37 (2020).
[15] See Supplemental Material at [URL] for additional details of the model, simulations, and computations including Figs. S1-S11.
[16] F. Brueckner and P. Cramer, Nat. Struct. Mol. Biol. **15**, 811 (2008).
[17] O. Bensaude, Transcription **2**, 103 (2011).
[18] H. Yin, M. D. Wang, K. Svoboda, R. Landick, S. M. Block, and J. Gelles, Science **270**, 1653 (1995).
[19] M. D. Wang, M. J. Schnitzer, H. Yin, R. Landick, J. Gelles, and S. M. Block, Science **282**, 902 (1998).
[20] D. Hnisz, K. Shrinivas, R. A. Young, A. K. Chakraborty, and P. A. Sharp, Cell **169**, 13 (2017).
[21] W.-K. Cho, J.-H. Spille, M. Hecht, C. Lee, C. Li, V. Grube, and I. I. Cisse, Science **361**, 412 (2018).
[22] S. Chong, C. Dugast-Darzacq, Z. Liu, P. Dong, G. M. Dailey, C. Cattoglio, A. Heckert, S. Banala, L. Lavis, X. Darzacq, and R. Tjian, Science **361**, eaar2555 (2018).
[23] T. H. S. Hsieh, C. Cattoglio, E. Slobodyanyuk, A. S. Hansen, O. J. Rando, R. Tjian, and X. Darzacq, Mol. Cell **78**, 539 (2020).
[24] Y. Jiang, J. Huang, K. Lun, B. Li, H. Zheng, Y. Li, R. Zhou, W. Duan, C. Wang, Y. Feng, H. Yao, C. Li, and X. Ji, Genome Biol **21**, 158 (2020).
[25] M. L. Huggins, J. Chem. Phys. **9**, 440 (1941).
[26] P. J. Flory, J. Chem. Phys. **9**, 660 (1941).
[27] S. S. Rao, M. H. Huntley, N. C. Durand, E. K. Stamenova, I. D. Bochkov, J. T. Robinson, A. L. Sanborn, I. Machol, A. D. Omer, E. S. Lander, and E. L. Aiden, Cell **159**, 1665 (2014).
[28] V. Bianco, E. Locatelli, and P. Malgaretti, Phys. Rev. Lett. **121**, 217802 (2018).

bioRxiv preprint doi: https://doi.org/10.1101/2022.04.30.490180; this version posted May 1, 2022. The copyright holder for this preprint (which was not certified by peer review) is the author/funder, who has granted bioRxiv a license to display the preprint in perpetuity. It is made available under aCC-BY-NC-ND 4.0 International license.



[29] S. Put, T. Sakaue, and C. Vanderzande, Phys. Rev. E **99**, 032421 (2019).
[30] M. Foglino, E. Locatelli, C. A. Brackley, D. Michieletto, C. N. Likos, and D. Marenduzzo, Soft Matter **15**, 5995 (2019).
[31] D. Saintillan, M. J. Shelley, and A. Zidovska, Proc. Natl. Acad. Sci. U.S.A. **115**, 11442 (2018).
[32] In real units, $\sigma = 0.07\mu$m and $\tau_B = \sigma^2/D_0 = 7 \times 10^{-4}$ s, where $D_0$ is the diffusion coefficient of a single locus [15].
[33] J. Kim, C. Kim, and B. J. Sung, Phys. Rev. Lett. **110**, 047801 (2013).
[34] L. Berthier and G. Biroli, Rev. Mod. Phys. **83**, 587 (2011).
[35] T. R. Kirkpatrick and D. Thirumalai, Rev. Mod. Phys. **87**, 183 (2015).
[36] T. R. Kirkpatrick and D. Thirumalai, Phys. Rev. A **37**, 4439 (1988).
[37] F. H. Stillinger and T. A. Weber, Science **225**, 983 (1984).
[38] D. Thirumalai, J. Phys. Chem. **93**, 5637 (1989).
[39] P. J. Steinhardt, D. R. Nelson, and M. Ronchetti, Phys. Rev. B **28**, 784 (1983).
[40] P. R. ten Wolde, M. J. Ruiz-Montero, and D. Frenkel, Phys. Rev. Lett. **75**, 2714 (1995).
[41] A. K. Omar, K. Klymko, T. Grandpre, and P. L. Geissler, Phys. Rev. Lett. **126**, 188002 (2021).
[42] H. W. Cho, G. Shi, T. R. Kirkpatrick, and D. Thirumalai, Phys. Rev. Lett. **126**, 137801 (2021).
[43] Y. Zhou, C. K. Hall, and M. Karplus, Phys. Rev. Lett. **77**, 2822 (1996).
[44] T. Nagano, Y. Lubling, C. Várnai, C. Dudley, W. Leung, Y. Baran, N. Mendelson Cohen, S. Wingett, P. Fraser, and A. Tanay, Nature **547**, 61 (2017).
[45] R. Landick, Biochem. Soc. Trans. **34**, 1062 (2006).
[46] G. L. Hager, J. G. McNally, and T. Misteli, Mol. Cell **35**, 741 (2009).